


Multiple Spoof Plasmonically Induced Transparency for Sensing Applications

Zhixia Xu^{1,2}, Yi Wang^{1,2}, Jie Chang^{1,2}, and Tie Jun Cui^{1,*}

¹State Key Laboratory of Millimeter Waves, Southeast University, Nanjing 210096, China

²School of Information Science and Technology, Dalian Maritime University, Dalian 116026, China

 (Received 28 March 2022; revised 30 May 2022; accepted 28 June 2022; published 11 August 2022)

We design a pair of resonators to realize multiple spoof plasmonically induced transparency (PIT) with high- Q group delays, which show potential in sensing applications. To reveal the mechanism of the multiple spoof PIT scheme, we deduce mathematical equations of a simplified model composed of multiple harmonic oscillators, and we further propose an equivalent-circuit model to analyze the metamaterials in an intuitive way. A prototype consisting of a broadband stub resonator and a spoof localized surface-plasmonic resonator is further fabricated to detect the complex permittivity of high-lossy liquids and solid samples in microwave bands. Experimental results show that the group-delay-based sensor can work well even when high-order modes are weakly excited, and the trade-off between sensitivity and properties of samples is discussed. The proposed double-resonator scheme with multiple spoof PIT is universal, and we design a metasurface working in terahertz bands to show that the concept can be widely used in various surface-sensing applications.

DOI: [10.1103/PhysRevApplied.18.024035](https://doi.org/10.1103/PhysRevApplied.18.024035)

I. INTRODUCTION

Based on the evanescent property of surface-plasmon polaritons (SPPs) on the surface of metallic films [1], localized surface-plasmonic (LSP) resonances are playing a crucial role in biological sensing to detect various biofluids, such as aqueous solutions of antibodies [2], drugs [3], proteins [4], and DNA [5]. SPP-based refractive-index (RI) sensing is advantageous because it is label free and can provide real-time information [6]. To realize SPP-like evanescent waves at lower frequencies, metallic structures decorated by periodic unit cells are found to support spoof SPPs with strong field confinement [7–11]. Furthermore, when adding periodic grooves to a resonator, we can realize multiple spoof LSP resonances [12–17] on the surface of a disk or fan-shaped resonator [18,19]. Spoof plasmonic metamaterials also show potential in sensing applications [20,21], where samples on the surface of metamaterials can be detected [22–26]. However, it is difficult to excite multiple LSP resonances with a high- Q factor due to the intrinsic damping in metallic structures [27,28]. Usually, only one LSP mode can be utilized to detect lossy liquids under test (LUT), and high-order modes are usually too weak for sensing [23]. To increase sensing performance, inserting gain components into spoof plasmonic structures is an effective method in microwave bands [29–32].

Plasmonically induced transparency (PIT) is an alternative way to realize high- Q resonances [33,34]. The

conventional double-resonator scheme usually generates one PIT window [35,36]. For example, a stub-coupled split-ring-resonator (SRR) sensor can detect permittivity at one transmission window [37]. Similar acoustically induced transparency [38–40] and exciton-induced transparency [41] based on double-resonance systems show only one transmission peak as well. To achieve multiple PIT windows, more resonators are needed, such as cascaded three nanodisk resonators [42], orthogonally oriented dipoles in the monomer and dimer bars [43], LSP coupled to electrical-magnetic dipoles [44], two open stubs coupled to four SRRs [45], and two-level atoms coupled to a single-mode cavity [46]. In this work, the proposed multiple spoof PIT scheme consists of one broadband stub resonator and one spoof LSP resonator. To describe the multiple spoof PIT transmission spectrum, we design a mechanical system composed of several harmonic oscillators to deduce mathematical equations, and we further propose an equivalent circuit to reveal the electromagnetic (EM) principle of metamaterials. A prototype is fabricated, and experiments conducted in microwave bands verify the sensing performance of the multiple spoof PIT, the group-delay spectrum of which shows a high- Q factor [47]. Complex permittivity of various samples was extracted based on the group delay. Moreover, the trade-off issue of sensitivity and permittivity is discussed. To show the generality of the scheme, we also design a metasurface working in terahertz bands. To sum up, this work finds a simple method to realize multiple spoof PIT, which is fruitful in sensing applications.

*tjcui@seu.edu.cn

II. SPOOF PIT, HARMONIC OSCILLATORS, AND EQUIVALENT CIRCUIT

The proposed multiple spoof PIT sensor is shown in Fig. 1(a). The wideband sector stub (bright mode) is connected to the microstrip line directly, and the spoof LSP resonator (dark-mode) is strongly coupled with the stub through the 0.2-mm-wide slot. The bandwidth of the sector stub is designed to be large enough to cover multiple spoof LSP resonances. Inspired by oscillator-coupling systems [48–50], we propose a mechanical model composed of harmonic oscillators, as shown in Fig. 1(b). Theoretical transmission equations deduced from the mechanical model are consistent with simulated results of the EM model in CST Studio Suite, as shown in Fig. 1(c).

Bright-mode oscillator 1 represents the wideband sector stub, and other dark-mode oscillators represent multiple spoof LSP modes. Oscillator 1 is subject to an external force, F . Mass, m_i , and springs attached to a wall with constant k_i decide the intrinsic resonant frequency, ω_i .

Springs k_{ij} connect different oscillators. Friction constant γ_i is associated with energy dissipation on these oscillators. We can write equations of oscillators in terms of the displacements, x_i , as follows:

$$\ddot{x}_1(t) + \gamma_1 \dot{x}_1(t) + \omega_1^2 x_1(t) - \frac{k_{21}}{m_1} x_2(t) - \frac{k_{31}}{m_1} x_3(t) - \frac{k_{41}}{m_1} x_4(t) = \frac{F}{m_1} e^{-i\omega_s t}, \quad (1)$$

$$\ddot{x}_2(t) + \gamma_2 \dot{x}_2(t) + \omega_2^2 x_2(t) - \frac{k_{21}}{m_2} x_1(t) = 0, \quad (2)$$

$$\ddot{x}_3(t) + \gamma_3 \dot{x}_3(t) + \omega_3^2 x_3(t) - \frac{k_{31}}{m_3} x_1(t) = 0, \quad (3)$$

$$\ddot{x}_4(t) + \gamma_4 \dot{x}_4(t) + \omega_4^2 x_4(t) - \frac{k_{41}}{m_4} x_1(t) = 0. \quad (4)$$

By substituting harmonic solutions into these equations, we can find the solution of x_1 as

$$x_1(t) = \frac{F e^{-i\omega_s t}}{m_1[(\omega_1^2 - \omega_s^2 - i\gamma_1\omega_s) - (\Omega_{21}^4/(\omega_2^2 - \omega_s^2 - i\gamma_2\omega_s)) - (\Omega_{31}^4/(\omega_3^2 - \omega_s^2 - i\gamma_3\omega_s)) - (\Omega_{41}^4/(\omega_4^2 - \omega_s^2 - i\gamma_4\omega_s))]}, \quad (5)$$

where coherent coupling between oscillators is $\Omega_{ij}^4 = k_{ij}^2/m_i m_j$. The absorbed power during one period can be further obtained as

$$P_s(\omega_s) = \frac{-2\pi i F^2 \omega_s}{m_1[(\omega_1^2 - \omega_s^2 - i\gamma_1\omega_s) - (\Omega_{21}^4/(\omega_2^2 - \omega_s^2 - i\gamma_2\omega_s)) - (\Omega_{31}^4/(\omega_3^2 - \omega_s^2 - i\gamma_3\omega_s)) - (\Omega_{41}^4/(\omega_4^2 - \omega_s^2 - i\gamma_4\omega_s))]} \quad (6)$$

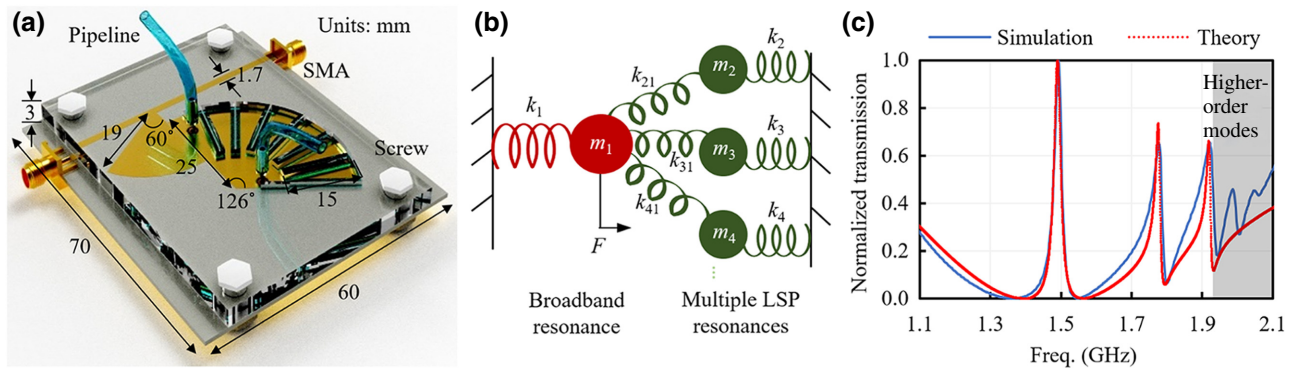


FIG. 1. (a) Multiple spoof PIT sensor. Substrate is Rogers 4350B, the thickness of which is 0.762 mm. Microfluidic structure is made of polycarbonate, the permittivity of which is 3 and the loss tangent is 0.05. Pipe is 0.2 mm from the spoof LSP structure. (b) Mechanical model with multiple transparent windows. (c) Theoretical and simulated results. Theoretical fitting parameters are $\gamma_1 = 8.164 \text{ N s m}^{-1}$, $\gamma_2 = 0.006 \text{ N s m}^{-1}$, $\gamma_3 = 0.031 \text{ N s m}^{-1}$, $\gamma_4 = 0.035 \text{ N s m}^{-1}$, $\Omega_{21} = 0.5 \times 2\pi \text{ rad s}^{-1}$, $\Omega_{31} = 0.46 \times 2\pi \text{ rad s}^{-1}$, $\Omega_{41} = 0.44 \times 2\pi \text{ rad s}^{-1}$, $\omega_1 = 1.49 \times 2\pi \text{ rad s}^{-1}$, $\omega_2 = 1.49 \times 2\pi \text{ rad s}^{-1}$, $\omega_3 = 1.78 \times 2\pi \text{ rad s}^{-1}$, $\omega_4 = 1.92 \times 2\pi \text{ rad s}^{-1}$, $F = 1 \text{ N}$, $m_1 = 1 \text{ kg}$.

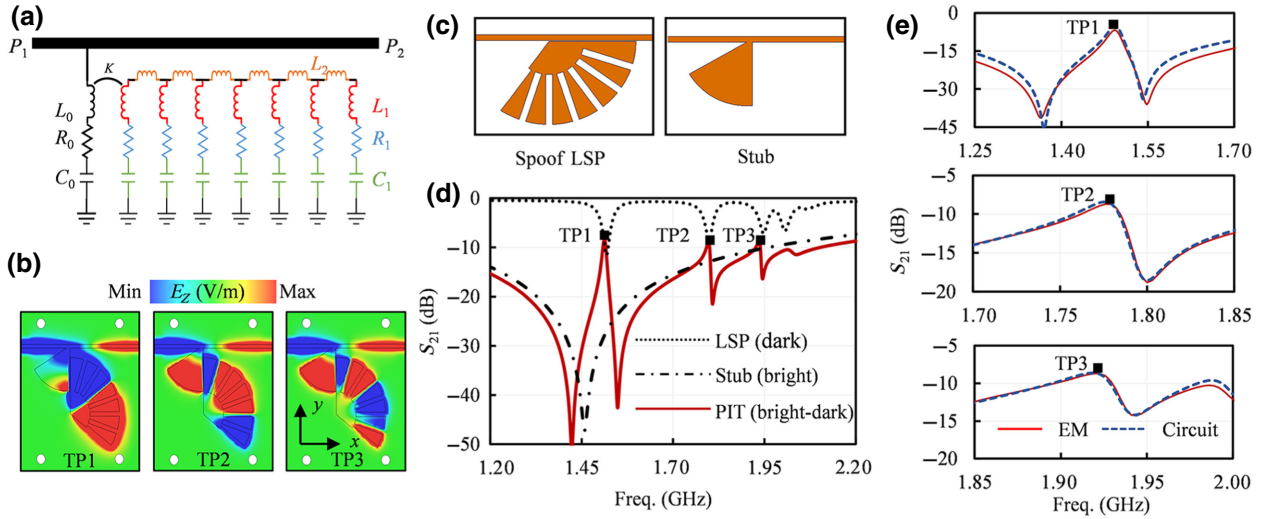


FIG. 2. (a) Equivalent spoof PIT circuit model. (b) Electric field distributions. (c) Simulation models to reveal bright and dark modes separately. (d) Simulated S_{21} curves of three models: spoof LSP, stub, and spoof PIT. (e) Comparison between the equivalent-circuit model and EM model.

We further define the normalized transmission spectrum, $T = 1 - \text{Re}(P_s)$, to conduct a curve fitting with the EM model in Fig. 1(c). The consistency between the theoretical model and simulations proves the correctness of the theory. More higher-order modes appear in the EM model, and we can increase the number of oscillators to get more precise equations. However, four oscillators are enough to describe the first three spoof PIT windows, which are utilized in subsequent experiments.

We further propose an equivalent circuit to demonstrate the working principle, as shown in Fig. 2(a). The bright-mode sector stub is treated as a LCR -series resonator (L_0 , C_0 , and R_0) connected to the main transmission line directly. The dark-mode spoof LSP resonator is treated as a section of open-terminal periodic transmission line with seven LCR -series resonators (L_1 , C_1 , and R_1) connected by the inductor L_2 . Coupling coils are used to present the coupling, K , between two resonators. Field distributions in Fig. 2(b) verify that spoof LSP resonances are strongly coupled with the sector stub resonator. To reveal the bright and dark modes separately, we establish two models shown in Fig. 2(c) and compare S_{21} curves of the two individual resonators with the S_{21} curve of spoof PIT in Fig. 2(d). The Q factor of the bright-mode stub resonator is much lower than that of the dark-mode spoof LSP resonator. Spoof LSP resonances appear more

densely when the frequency increases closer to the cutoff frequency, ω_c . When two resonators are coupled together, discrete spoof PIT transmission peaks (TPs) appear at the location of dark-mode spoof LSP resonances. To extract equivalent-circuit parameters, we combine curve-fitting optimization with physical-insight analysis. We first analyze the sector stub and the spoof LSP resonator separately to determine fundamental relationships according to the resonant frequencies and Q factor. The resonant frequency of a single groove is about the cutoff frequency, ω_c . Then, we use the quasi-Newton optimization tool to get all fitting parameters. Considering the difference of K of different modes, we separately analyze the equivalent circuit at different spoof PIT windows, as shown in Fig. 2(e). Results of the equivalent circuit match well with EM simulations. Detailed parameters are listed in Table I.

III. MEASUREMENT

A. Fabrication and measurement setup

As shown in Fig. 3(a), the proposed sensor is fabricated, and measurements are conducted to verify its performance. The microfluidic structure is made of polycarbonate. A pair of plastic tubes is connected to the inlet and outlet ports of the microfluidic chip. A syringe is used to pump

TABLE I. Parameters of the equivalent-circuit model at different TPs.

Parameters	L_0 (nH)	L_1 (nH)	L_2 (nH)	C_0 (pF)	C_1 (pF)	R_0 (Ω)	R_1 (Ω)	K
TP1	1.9	19.6	4	6.36	0.29	0.074	2.6	0.30
TP2	1.7	18.8	6.2	6.36	0.30	0.074	3.0	0.18
TP3	1.7	18.5	6.5	6.36	0.30	0.074	3.2	0.17

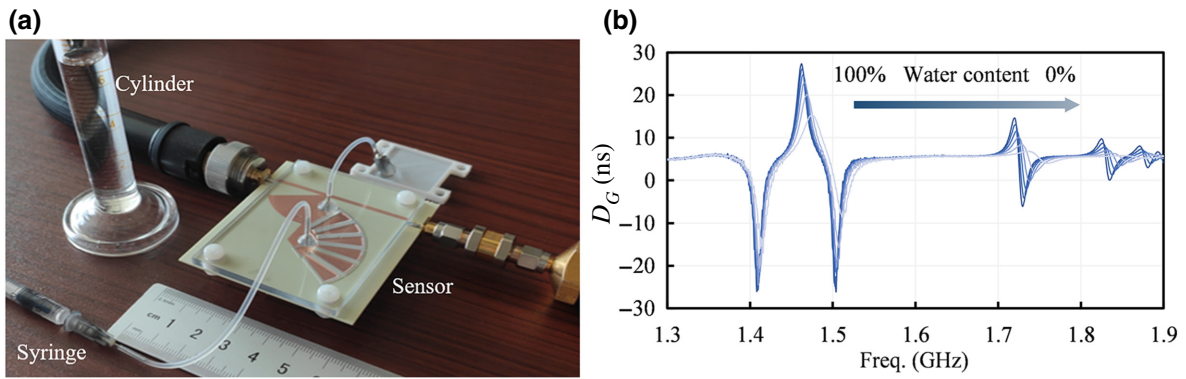


FIG. 3. (a) Experiment environment. Room temperature is 28 °C. Volume of LUT is 0.2 ml in the microfluidic pipe. (b) Measured group delay of different water-ethanol solutions.

the LUT into the tube, and the waste liquid is collected from the outlet port. Two terminals are welded with connectors, linked with the vector network analyzer (Agilent N5230A), the intermediate frequency bandwidth of which is set as 10 kHz. Figure 3(b) shows some measured results of different water-ethanol solutions. As the water content decreases, the real part of the permittivity decreases, and the imaginary part of the permittivity increases [51]; therefore, the measured group-delay peaks shift towards higher frequency and the amplitude decreases.

B. Calibration using water-ethanol solutions

We first calibrate the sensor based on water-ethanol solutions, the referential permittivities of which cover an extensive range. Figures 4(a)–4(c) show the peak frequency and group-delay change with water-content change at three TPs, respectively. With these experimental results, we further obtain the mathematical relationship between the group delay and permittivity of LUT. It is challenging to deduce rigorous physical relationships between samples and the parameters of sensors. Common calibrations are

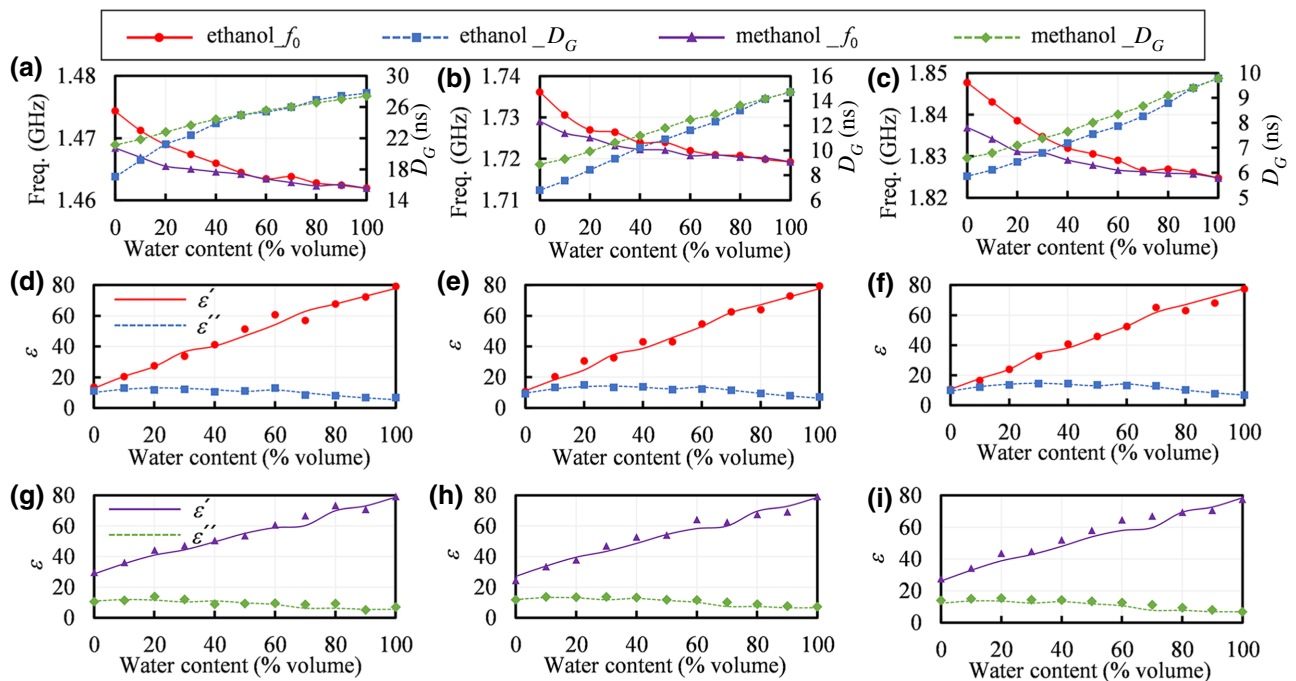


FIG. 4. Peak frequency (f_0) and group delay (D_G) of different water-ethanol and water-methanol solutions at (a) TP1, (b) TP2, and (c) TP3. Comparison of permittivity between the theoretical results (solid and dashed lines) of the Debye model and the measured results (discrete dots) of water-ethanol solutions at (d) TP1, (e) TP2, and (f) TP3, and water-methanol solutions at (g) TP1, (h) TP2, and (i) TP3.

TABLE II. Curve fitting of the spoof PIT spectrum and permittivity.

Fitting functions	$\varepsilon' = A/(B \times f_0^2 + C \times f_0 + D) + E$					$\varepsilon'' = F \times D_G + G \times f_0 + H$				
	<i>A</i>	<i>B</i>	<i>C</i>	<i>D</i>	<i>E</i>	<i>F</i>	<i>G</i>	<i>H</i>	$R^2(\varepsilon')$	$R^2(\varepsilon'')$
TP1	65.3	42.1	-25.1	-52.6	-21.2	-5.2	-4165.8	6241.2	0.97	0.82
TP2	69.1	30.0	-26.6	-42.2	-24.6	-2.6	-1102.6	1941.4	0.98	0.92
TP3	95.1	24.5	-25.3	-34.6	-29.4	-4.9	-695.5	1323.9	0.99	0.95

based on an empirical two-step process: choose mathematical equations and obtain parameters based on curve fitting [23]. Therefore, we use the curve-fitting equations in Table II to match relationships between the complex permittivity and group delay, where the peak frequency (f_0) and peak group delay (D_G) are used. ε' is the real part and ε'' is the imaginary part of the permittivity. Curve-fitting parameters are presented from *A* to *H*. When ε' increases, f_0 decreases as well. Moreover, D_G is related to the oscillation time of the strong coupling system, which has an approximative linear relationship with ε'' . Larger ε'' is related to a smaller D_G . To verify the correctness of the mathematical relationships, we use the curve-fitting toolbox in MATLAB to match measured results at three testing points with mathematical models. Obtained parameters and R^2 values are listed in Table II, where R^2 is a statistical parameter to evaluate how close data are to the fitted regression line. Figure 5(a) presents the fitting performance where measured results match the mathematical model well. We further compute the measured permittivity of water-ethanol solutions in Figs. 4(d)–4(f), where the theoretical values [51] match well with the extracted permittivity.

C. Validation using water-methanol solutions

Further characterization of other solutions is reliable based on the mathematical model deduced from water-ethanol solutions. We then measure water-methanol solutions as examples. Measured f_0 and D_G are plotted as

functions of the water volume fraction in Figs. 4(a)–4(c). The mathematical model obtained by the water-ethanol calibration is directly applied to measure water-methanol solutions. The theoretical results in Ref. [51] are compared with the measured results in Figs. 4(g)–4(i). The consistency verifies the accuracy of the developed sensor. We further use the following equation to evaluate the relative error:

$$\text{error} = \frac{1}{N} \sum_{i=0}^N \frac{|\varepsilon_m(i) - \varepsilon_t(i)|}{\varepsilon_t(i)} \times 100\%, \quad (7)$$

where i represents different solutions from pure water to pure methanol with a step of 10% water content. N represents 11 sets of data in total. ε_m and ε_t are the measured and theoretical permittivity, respectively [51]. Relative errors of ε' are 4.32%, 5.11%, and 6.30%, and relative errors of ε'' are 17.80%, 11.60%, and 16.26% from TP1 to TP3, respectively. Based on the Debye model [51], we calculate the theoretical loss tangent of different solutions, as shown in Fig. 5(b). The loss tangent at the TP1 is slightly lower than the results at TP2 and TP3. The same change is revealed by our experimental results shown in Fig. 5(c).

IV. DISCUSSION

A. Group delay and *S* parameters

Group delay could be a better parameter than the *S* parameters for spoof PIT sensors because it can reveal bidirectional energy transfer between resonators. To utilize

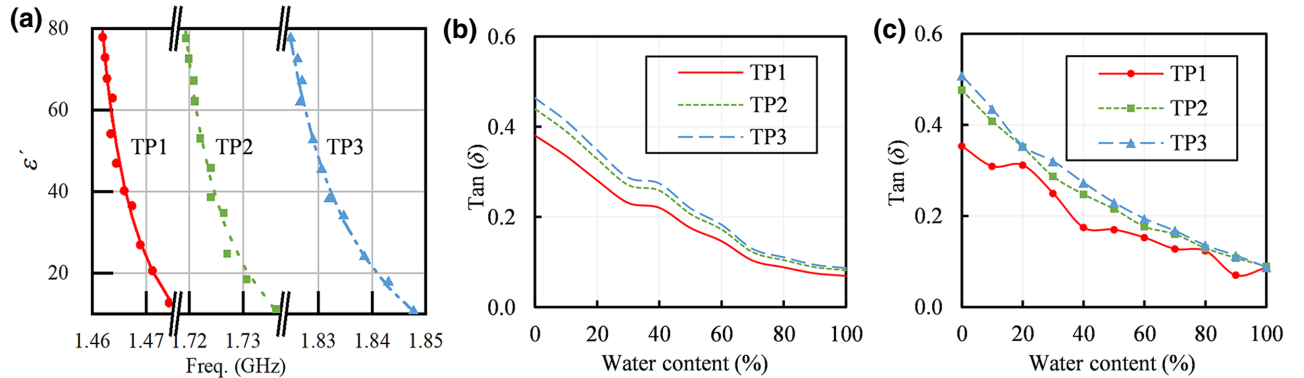


FIG. 5. (a) Fitting performance of ε' and f_0 , where lines are fitting curves of the mathematical model and dots are measured results. (b) Loss tangent ($\tan \delta$) of theoretical results. (c) $\tan \delta$ of measured results.

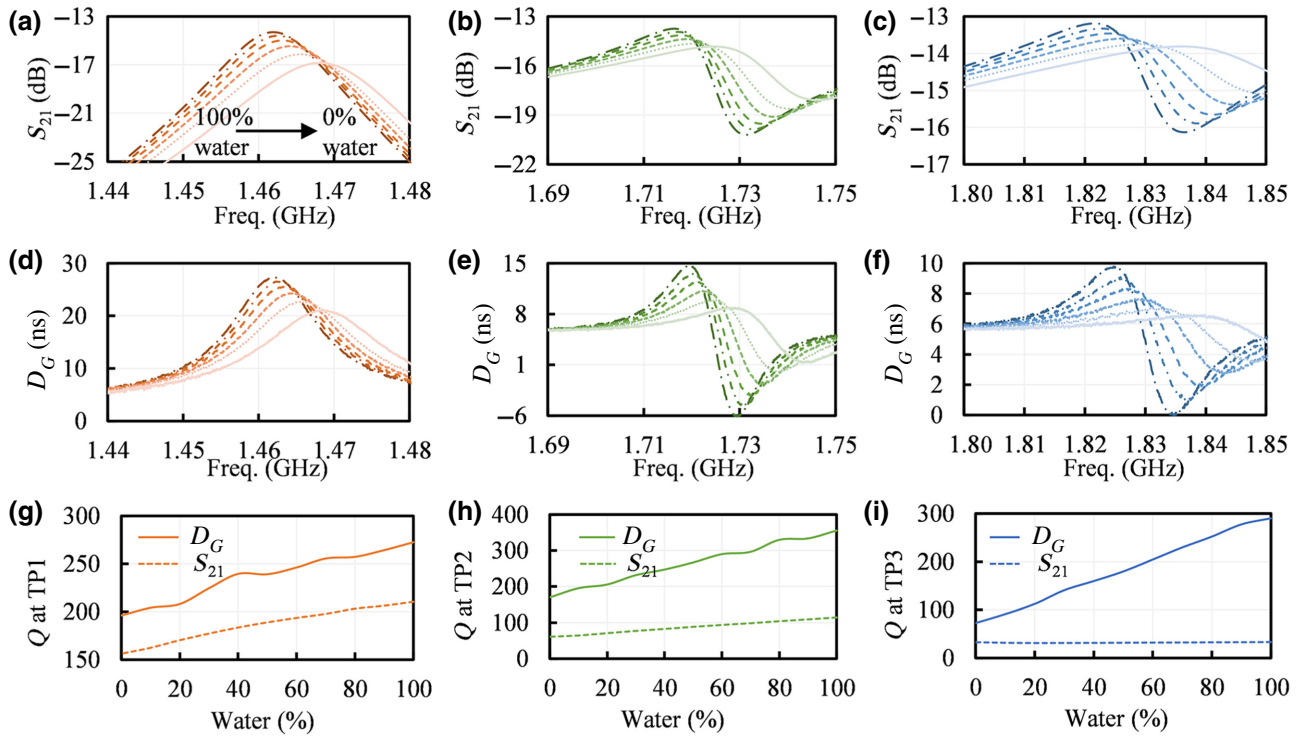


FIG. 6. Experimental comparison between S_{21} and group delay around three TPs with various solutions. (a)–(c) S_{21} curves. (d)–(f) Group-delay curves. (g)–(i) Comparison of Q factor of S_{21} and group delay.

higher-order spoof LSP resonances in this strong coupling scheme, we use group delay as a sensing parameter instead of conventional S parameters. S_{21} of our design can work well at TP1; however, it becomes difficult to identify at higher-order modes, such as TP2 and TP3. As shown in the enlarged spectrum at TP3 in Fig. 6(c), the change in amplitude of S_{21} is not clear enough to use, where the peak range is from -13.25 to -13.75 dB, with a scale of about 0.5 dB. As a comparison in Fig. 6(f), the peak range of the group delay is from 6 to 10 ns, which can be used for measurements.

From the perspective of the physical mechanism, using group delay is reasonable in spoof PIT-sensing systems. Once the coupling becomes sufficiently large, the group delay reveals the bouncing time between resonant modes. The complex permittivity of the LUT affects both the resonant frequency and group delay. Therefore, it is natural to consider the frequency and group delay as a pair of optional parameters. The mathematical definition of group delay is $D_G = -d\varphi/d\omega$. Suppose we know S_{21} at two different frequencies, f_1 and f_2 , which are very close to each other, $D_G \approx -\text{phase}[S_{21}(f_1) - S_{21}(f_2)]/[2\pi(f_1 - f_2)]$. Group delay is a parameter based on a differential operation with frequency. Therefore, group delay indicates the change rate with frequency, meaning that, when the amplitude of S_{21} is low, the change rate with frequency can still be significant. In the spoof PIT scheme, the advantage of group delay can be reflected in the sharpness. Because the change of S_{21}

is weak, we cannot obtain the $Q_{-3\text{dB}}$ factor based on the 3-dB bandwidth of S_{21} . Thus, we define the $Q_{-1\text{dB}}$ factor to describe the sharpness of curves as $Q_{-1\text{dB}} = f_0/(f_2 - f_1)$, where f_0 is the resonant peak frequency, and f_2 and f_1 are frequencies on both sides at which the amplitude decreases to 0.89 times. From Figs. 6(a)–6(c), higher $Q_{-1\text{dB}}$ verifies that group-delay curves are sharper than S_{21} curves at all three TPs. Hence, group delay can be a better sensing parameter than the amplitude of S_{21} in spoof PIT sensors, and the conclusion is universal for other sensors based on strong coupling.

B. Trade-off between sensitivity and permittivity

Sensitivity is used to characterize the frequency-shift ability when detecting samples. When detecting a lossy LUT with a large range of high permittivity, we use the microfluidic structure and sacrifice sensitivity to maintain the function of the sensor. However, when detecting samples with low permittivity, such as glass and Teflon, we place samples on the surface of metamaterials directly and achieve a high sensitivity. Two different situations are compared in Fig. 7(a). The trade-off between sensitivity and samples is discussed in this section.

The sensitivity is a complex function with many variables, such as permittivity, the working frequency, and the test environment. The following definition reveals the

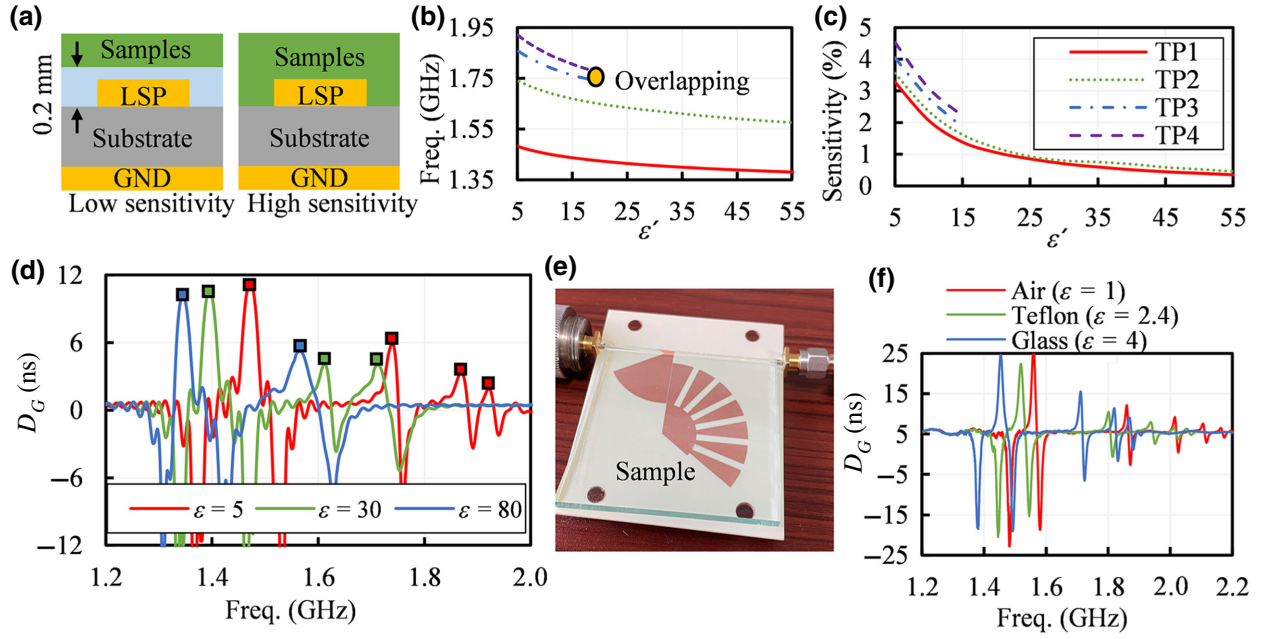


FIG. 7. Trade-off between sensitivity and samples. (a) Low sensitivity, there is a gap between samples and spoof LSP. High sensitivity, samples are placed on the surface of spoof LSP directly. Spoof LSP is etched on the up-layer surface of the substrate, and metallic ground (GND) is etched on the bottom-layer surface of the substrate. (b) Frequency shift of different modes. (c) Sensitivity of different modes. (d) Spectra of various samples, and mode overlapping occurs in green and blue curves. (e) Experiments to detect samples with low permittivity. (f) Measured group delay of different samples with low permittivity.

frequency-shifting ability with the change in permittivity:

$$S(\varepsilon) = \frac{\partial f_0}{f_{\text{air}} \partial \varepsilon'}, \quad (8)$$

where the sensitivity (S) is regarded as a function of the resonant frequency (f_0) and the real part of the permittivity (ε'). The cross section of our sensor with high sensitivity is shown in Fig. 7(a), where samples are placed directly on the surface of the structure. We simulate the frequency shift of various spoof PIT modes when the permittivity of the sample changes over a large scale. The third and fourth spoof PIT modes overlap in Fig. 7(b) because of the inconsistent sensitivity at various spoof PIT modes, as shown in Fig. 7(c). Higher-order spoof PIT modes have higher sensitivity because of the tighter confinement of the electric field. In the spectrum shown in Fig. 7(d), we can clearly see

four spoof PIT peaks when the permittivity of the sample is 5; however, only two peaks exist when the permittivity increases to 80. These results prove that sensitivity is not a parameter that can be increased at will, especially when designing a multimode sensor.

When we detect samples with low permittivity, such as glass and Teflon shown in Fig. 7(e), the sensitivity can be much higher than that of prior experiments. We list various recent spoof plasmonic sensors in Table III based on the definition of normalized sensitivity presented in Ref. [23]. We can see that the proposed sensor based on multiple spoof PIT can achieve high sensitivity when detecting samples with low permittivity. To sum up, the distance between the sample and the spoof LSP resonator tunes the sensitivity. In a previously fabricated sensor with a microfluidic pipe, the distance is 0.2 mm, and gradual frequency shifting without any mode overlap can

TABLE III. Various spoof plasmonic sensors in microwave bands.

Ref.	Structure	Num. of Modes	Size (mm ³)	Sensitivity (%)	Samples
[25]	Spoof SPP	4	240 × 25 × 0.787	0.34	Substrate
[26]	Spoof SPP	1	20 × 10 × 0.15	...	Glucose
[24]	Spoof LSP	2	100 × 70 × 1.52	...	Glucose
[21]	Spoof LSP	1	40 × 32 × 2.5	0.04	Ethanol
[23]	Spoof LSP	1	20 × 15 × 0.254	0.57	Ethanol
[29]	Spoof LSP	1	40 × 42 × 0.508	0.30	Glucose
This work	Spoof LSP	3	60 × 70 × 0.762	0.06 4.40	Ethanol/methanol Teflon/glass

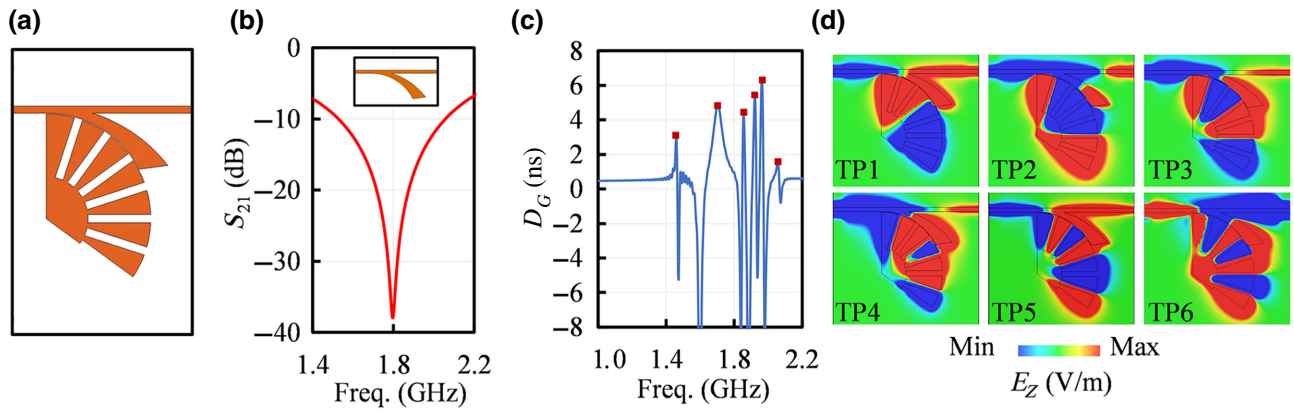


FIG. 8. (a) Structure with better performance of high-order modes. (b) Performance of the arc-shaped stub, the center frequency of which overlaps with the high-order spoof LSP modes. (c) Spoof PIT group delay. (d) Field distributions.

be observed in Fig. 3(b). When decreasing the space or directly placing the sample on the surface of the metamaterials, we can increase the sensitivity. High sensitivity is beneficial to detect samples with low permittivity, but, when meeting lossy and dispersive LUT with high permittivity, the sensor may not work well.

C. Enhancing higher-order modes

In the structure in Fig. 3, high-order spoof PIT modes are weakly excited. In this section, we adjust the structure to enhance the higher-order modes, as illustrated in Fig. 8(a). The basic mechanism relies on the center frequency of the broadband bright-mode stub. Although the bandwidths of both stubs shown in Figs. 2(c) and 8(b) are large enough to cover multiple spoof LSP resonances, different center frequencies mean that the strongest bright-mode excitation positions are different. When we adjust the center frequency of the bright mode to match better with the higher-order spoof LSP modes, the performance of higher-order modes becomes better, as shown in Fig. 8(c). In addition to the center frequency of the bright mode, the shape of the stub matters. The higher-order spoof LSP modes have stronger fields along the periodic grooves, and the arc-shaped stub can couple these modes better than the fan-shaped stub placed near the terminal of the spoof LSP resonator. To confirm the existence of higher-order spoof PIT modes, we plot field distributions, as shown in Fig. 8(d).

D. Metasurfaces

To confirm the generality of the proposed multiple spoof PIT scheme, we further design a silver (Ag) metasurface working in terahertz bands. The 100-nm-thick Ag structure is etched on both surfaces of a 25- μm -thick polyimide substrate, as shown in Fig. 9(a), and the metasurface is practical for fabrication, similar to a recently reported SRR surface with electromagnetically induced transparency [52].

The intrinsic property of Ag is modeled as a lossy metal with a conductivity of 6.3×10^7 S/m, and the polyimide film is treated as a dielectric ($\epsilon_{\text{sub}} = 3.3 + i0.015$), and we conduct simulations using the CST Studio Suite. We first analyze two resonators separately under the excitation of plane waves to investigate the bandwidth of resonances based on the cross section in Fig. 9(b) to confirm that the broadband dipole mode covers multiple spoof LSP modes; then, we arrange two resonators together to construct a multiple spoof PIT coupling scheme, where the elliptical dipole patch is bent to enhance the coupling with spoof LSP modes. Multiple spoof PIT windows appear in the spectrum, as shown in Fig. 9(c), and corresponding electric field distributions at TPs are presented in Fig. 9(d) to verify the coupling effect. If we change the RI of the 1- μm -thick dielectric samples on the surface, the transmission windows shift, indicating the surface-sensing applications [53–55]. It is challenging to realize these higher-order PIT modes in optical bands because of the high metallic damping. We conduct parameter analyses of the metallic conductivity (σ), as shown in Fig. 9(e). Damping affects the higher-order modes more severely than the fundamental mode because the Ohmic loss is proportional to σE^2 . Higher-order plasmonic modes have stronger field confinements, meaning a stronger E and larger damping.

V. CONCLUSION

We realize multiple spoof PIT based on a pair of broadband and spoof LSP resonators. A coupling system consisting of multiple harmonic oscillators is proposed to deduce a precise mathematical equation to describe the multiple spoof PIT spectrum. We also propose an equivalent-circuit model to qualitatively describe the mechanism. A spoof PIT sensor is further fabricated to detect the complex permittivity of lossy LUT. Experiments in microwave bands validate the precise and stable sensing ability based on the sharp group-delay spectrum. It should be mentioned

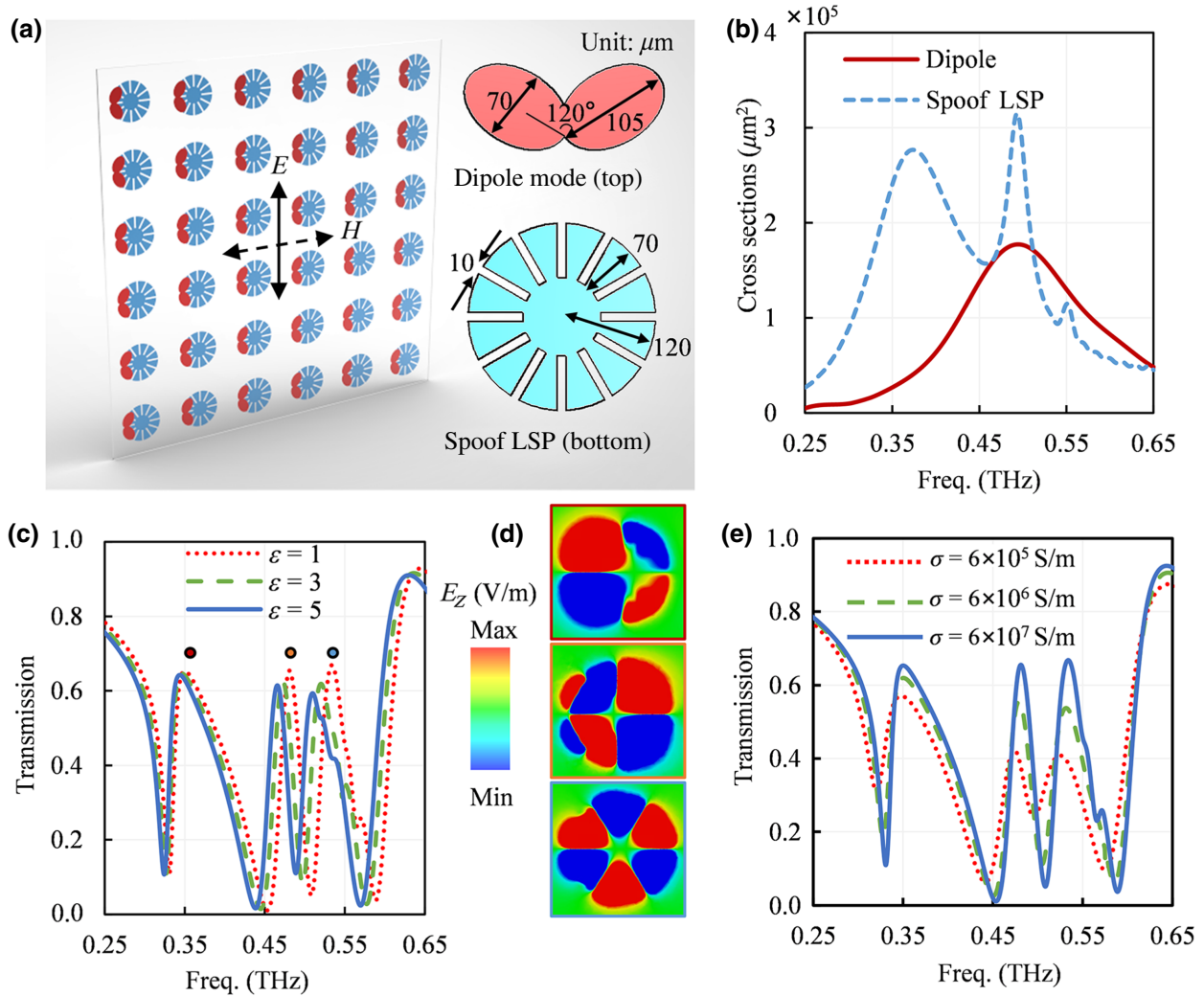


FIG. 9. (a) Multiple spoof PIT metasurface with two-layer structures working in terahertz bands. (b) Cross sections of two resonators. (c) Transmission spectrum with different 1- μm -thick samples on the surface. Field distributions at different spoof PIT windows. (d) Performance with different conductivity.

that the desynchronization of the frequency shift may cause mode overlapping and finally disable the sensor; thus, we cannot pursue very high sensitivity when designing multimode sensors to detect samples for which the RI changes over a large range. Further experiments verify that our design can achieve higher sensitivity when detecting low-loss samples with small permittivity. The proposed multiple spoof PIT scheme is universal technology in microwave and terahertz bands, and we design a metasurface as an example.

ACKNOWLEDGMENTS

T.J.C. acknowledges support from the National Key Research and Development Program of China (Grants No. 2017YFA0700201, No. 2017YFA0700202, and No. 2017YFA0700203). This work is also supported by the State Key Laboratory of Millimeter Waves under Grant

No. K202202 and the Fundamental Research Funds for the Central Universities under Grant No. 3132022240.

All the authors have accepted responsibility for the entire content of this submitted manuscript and approved submission.

The authors declare no conflicts of interest regarding this article.

[1] S. A. Maier, *Plasmonics: Fundamentals and Applications* (Springer Science & Business Media, New York, 2007).
 [2] H. Im, H. Shao, Y. I. Park, V. M. Peterson, C. M. Castro, R. Weissleder, and H. Lee, Label-free detection and molecular profiling of exosomes with a nano-plasmonic sensor, *Nat. Biotechnol.* **32**, 5 (2014).
 [3] Y. Wang, C. Zhao, J. Wang, X. Luo, L. Xie, S. Zhan, J. Kim, X. Wang, X. Liu, and Y. Ying, *Wearable*

- plasmonic-metamaterial sensor for noninvasive and universal molecular fingerprint detection on biointerfaces, *Sci. Adv.* **7**, eabe4553 (n.d.).
- [4] D. Rodrigo, O. Limaj, D. Janner, D. Etezadi, F. J. García de Abajo, V. Pruneri, and H. Altug, Mid-infrared plasmonic biosensing with graphene, *Science* **349**, 165 (2015).
- [5] M. Dass, F. N. Gür, K. Kołataj, M. J. Urban, and T. Liedl, DNA origami-enabled plasmonic sensing, *J. Phys. Chem. C* **125**, 5969 (2021).
- [6] S.-H. Oh, H. Altug, X. Jin, T. Low, S. J. Koester, A. P. Ivanov, J. B. Edel, P. Avouris, and M. S. Strano, Nanophotonic biosensors harnessing van der Waals materials, *Nat. Commun.* **12**, 3824 (2021).
- [7] J. B. Pendry, A. J. Holden, W. J. Stewart, and I. Youngs, Extremely Low Frequency Plasmons in Metallic Mesostructures, *Phys. Rev. Lett.* **76**, 4773 (1996).
- [8] J. B. Pendry, L. Martín-Moreno, and F. J. Garcia-Vidal, Mimicking surface plasmons with structured surfaces, *Science* **305**, 847 (2004).
- [9] J. B. Pendry, P. A. Huidobro, Y. Luo, and E. Galiffi, Compacted dimensions and singular plasmonic surfaces, *Science* **358**, 915 (2017).
- [10] Z. Gao, L. Wu, F. Gao, Y. Luo, and B. Zhang, Spoof plasmonics: From metamaterial concept to topological description, *Adv. Mater.* **30**, 1706683 (2018).
- [11] F. J. Garcia-Vidal, A. I. Fernandez-Dominguez, L. Martín-Moreno, H. C. Zhang, W. Tang, R. Peng, and T. J. Cui, Spoof surface plasmon photonics, *Rev. Mod. Phys.* **94**, 025004 (2022).
- [12] X. Shen and T. J. Cui, Ultrathin plasmonic metamaterial for spoof localized surface plasmons, *Laser Photonics Rev.* **8**, 137 (2014).
- [13] P. A. Huidobro, X. Shen, J. Cuerda, E. Moreno, L. Martín-Moreno, F. J. Garcia-Vidal, T. J. Cui, and J. B. Pendry, Magnetic localized surface plasmons, *Phys. Rev. X* **4**, 021003 (2014).
- [14] W. X. Tang, H. C. Zhang, H. F. Ma, W. X. Jiang, and T. J. Cui, Concept, theory, design, and applications of spoof surface plasmon polaritons at microwave frequencies, *Adv. Opt. Mater.* **7**, 1800421 (2019).
- [15] Z. Liao, X. Shen, B. C. Pan, J. Zhao, Y. Luo, and T. J. Cui, Combined system for efficient excitation and capture of LSP resonances and flexible control of SPP transmissions, *ACS Photonics* **2**, 738 (2015).
- [16] X. Shen, T. J. Cui, D. Martín-Cano, and F. J. Garcia-Vidal, Conformal surface plasmons propagating on ultrathin and flexible films, *Proc. Natl. Acad. Sci.* **110**, 40 (2013).
- [17] H. F. Ma, X. Shen, Q. Cheng, W. X. Jiang, and T. J. Cui, Broadband and high-efficiency conversion from guided waves to spoof surface plasmon polaritons, *Laser Photonics Rev.* **8**, 146 (2014).
- [18] Z. Xu, S. Li, Y. Liu, H. Zhao, and X. Yin, Characteristic mode analysis of complex spoof localized surface plasmon resonators, *IEEE Access* **6**, 2871 (2018).
- [19] Z. Li, L. Liu, A. I. Fernández-Domínguez, J. Shi, C. Gu, F. J. García-Vidal, and Y. Luo, Mimicking localized surface plasmons with structural dispersion, *Adv. Opt. Mater.* **7**, 1900118 (2019).
- [20] X. Zhang, W. Y. Cui, Y. Lei, X. Zheng, J. Zhang, and T. J. Cui, Spoof localized surface plasmons for sensing applications, *Adv. Mater. Technol.* **6**, 2000863 (2021).
- [21] L. H. Dai, H. Z. Zhao, X. Zhao, and Y. J. Zhou, Flexible and printed microwave plasmonic sensor for noninvasive measurement, *IEEE Access* **8**, 163238 (2020).
- [22] R. L. Shao, Y. J. Zhou, and L. Yang, Quarter-mode spoof plasmonic resonator for a microfluidic chemical sensor, *Appl. Opt.* **57**, 8472 (2018).
- [23] Q. Jiang, Y. Yu, Y. Zhao, Y. Zhang, L. Liu, and Z. Li, Ultra-compact effective localized surface plasmonic sensor for permittivity measurement of aqueous ethanol solution with high sensitivity, *IEEE Trans. Instrum. Meas.* **70**, 1 (2021).
- [24] N. Pandit, R. K. Jaiswal, and N. P. Pathak, Plasmonic metamaterial-based label-free microfluidic microwave sensor for aqueous biological applications, *IEEE Sens. J.* **20**, 10582 (2020).
- [25] W. Y. Cui, J. Zhang, X. Gao, X. Zhang, and T. J. Cui, Passive amplitude-phase modulations and sensing based on Mach–Zehnder interferometer of spoof surface plasmon polaritons, *J. Opt.* **23**, 075101 (2021).
- [26] A. Kandwal, L. W. Liu, T. Igbe, J. Li, Y. Liu, R. Das, B. K. Kanaujia, L. Wang, and Z. Nie, A novel method of using bifilar spiral resonator for designing thin robust flexible glucose sensors, *IEEE Trans. Instrum. Meas.* **70**, 1 (2021).
- [27] B. Wang, P. Yu, W. Wang, X. Zhang, H.-C. Kuo, H. Xu, and Z. M. Wang, High- Q plasmonic resonances: Fundamentals and applications, *Adv. Opt. Mater.* **9**, 2001520 (2021).
- [28] Z. Xu, S. Li, X. Yin, H. Zhao, and L. Liu, Radiation loss of planar surface plasmon polaritons transmission lines at microwave frequencies, *Sci. Rep.* **7**, 6098 (2017).
- [29] H. Z. Zhao, Y. J. Zhou, J. Cai, Q. Y. Li, Z. Li, and Z. Y. Xiao, Ultra-high resolution sensing of glucose concentration based on amplified half-integer localized surface plasmons mode, *J. Phys. D: Appl. Phys.* **53**, 095305 (2019).
- [30] Y. J. Zhou, Q. Y. Li, H. Z. Zhao, and T. J. Cui, Gain-assisted active spoof plasmonic Fano resonance for high-resolution sensing of glucose aqueous solutions, *Adv. Mater. Technol.* **5**, 1900767 (2020).
- [31] J. Cai, Y. J. Zhou, Y. Zhang, and Q. Y. Li, Gain-assisted ultra-high- Q spoof plasmonic resonator for the sensing of polar liquids, *Opt. Express* **26**, 25460 (2018).
- [32] X. Gao, J. Zhang, Y. Luo, Q. Ma, G. D. Bai, H. C. Zhang, and T. J. Cui, Reconfigurable parametric amplifications of spoof surface plasmons, *Adv. Sci.* **8**, 2100795 (2021).
- [33] S. Zhang, D. A. Genov, Y. Wang, M. Liu, and X. Zhang, Plasmon-Induced Transparency in Metamaterials, *Phys. Rev. Lett.* **101**, 047401 (2008).
- [34] D. Hasan, C. P. Ho, and C. Lee, Thermally tunable absorption-induced transparency by a quasi 3D bow-tie nanostructure for nonplasmonic and volumetric refractive index sensing at mid-IR, *Adv. Opt. Mater.* **4**, 943 (2016).
- [35] Z. Xu, S. Liu, S. Li, and X. Yin, Analog of electromagnetically induced transparency based on magnetic plasmonic artificial molecules with symmetric and antisymmetric states, *Phys. Rev. B* **99**, 041104(R) (2019).
- [36] N. Liu, T. Weiss, M. Mesch, L. Langguth, U. Eigenthaler, M. Hirscher, C. Sonnichsen, and H. Giessen, Planar metamaterial analogue of electromagnetically induced transparency for plasmonic sensing, *Nano Lett.* **10**, 1103 (2010).
- [37] Z. Xu, Y. Wang, and S. Fang, Dielectric characterization of liquid mixtures using EIT-like transmission window, *IEEE Sens. J.* **21**, 17859 (2021).

- [38] Y. Cheng, Y. Jin, Y. Zhou, T. Hao, and Y. Li, Distinction of Acoustically Induced Transparency and Autler-Townes Splitting by Helmholtz Resonators, *Phys. Rev. Appl.* **12**, 044025 (2019).
- [39] Y. Liu, A. Talbi, E. H. E. Boudouti, O. B. Matar, P. Pernod, and B. Djafari-Rouhani, Autler-Townes Splitting and Acoustically Induced Transparency Based on Love Waves Interacting with a Pillared Metasurface, *Phys. Rev. Appl.* **11**, 064066 (2019).
- [40] M. Oudich, B. Djafari-Rouhani, B. Bonello, Y. Pennec, S. Hemaïdia, F. Sarry, and D. Beyssen, Rayleigh Waves in Phononic Crystal Made of Multilayered Pillars: Confined Modes, Fano Resonances, and Acoustically Induced Transparency, *Phys. Rev. Appl.* **9**, 034013 (2018).
- [41] T. V. Shahbazyan, Exciton-induced transparency in hybrid plasmonic systems, *Phys. Rev. B* **102**, 205409 (2020).
- [42] H. Lu, X. Liu, and D. Mao, Plasmonic analog of electromagnetically induced transparency in multi-nanoresonator-coupled waveguide systems, *Phys. Rev. A* **85**, 053803 (2012).
- [43] G. Rana, P. Deshmukh, S. Palkhivala, A. Gupta, S. P. Duttagupta, S. S. Prabhu, V. Achanta, and G. S. Agarwal, Quadrupole-Quadrupole Interactions to Control Plasmon-Induced Transparency, *Phys. Rev. Appl.* **9**, 064015 (2018).
- [44] S. Liu, Z. Xu, X. Yin, and H. Zhao, Analog of multiple electromagnetically induced transparency using double-layered metasurfaces, *Sci. Rep.* **10**, 8469 (2020).
- [45] Z. Chen, X. Q. Lin, Y. H. Yan, F. Xiao, M. T. Khan, and S. Zhang, Noncontact group-delay-based sensor for metal deformation and crack detection, *IEEE Trans. Ind. Electron.* **68**, 7613 (2021).
- [46] K. Ullah, H. Jing, and F. Saif, Multiple electromechanically-induced-transparency windows and Fano resonances in hybrid nano-electro-optomechanics, *Phys. Rev. A* **97**, 033812 (2018).
- [47] V. Krivenkov, S. Goncharov, I. Nabiev, and Y. P. Rakovich, Induced transparency in plasmon–exciton nanostructures for sensing applications, *Laser Photonics Rev.* **13**, 1800176 (2019).
- [48] L. Novotny, Strong coupling, energy splitting, and level crossings: A classical perspective, *Am. J. Phys.* **78**, 1199 (2010).
- [49] C. L. G. Alzar, M. A. G. Martinez, and P. Nussenzeig, Classical analog of electromagnetically induced transparency, *Am. J. Phys.* **70**, 5 (2002).
- [50] M. Baraclough, I. R. Hooper, and W. L. Barnes, Investigation of the coupling between tunable split-ring resonators, *Phys. Rev. B* **98**, 085146 (2018).
- [51] J. Bao, M. L. Swicord, and C. C. Davis, Microwave dielectric characterization of binary mixtures of water, methanol, and ethanol, *J. Chem. Phys.* **104**, 4441 (1996).
- [52] R. Yahiaoui, J. A. Burrow, S. M. Mekonen, A. Sarangan, J. Mathews, I. Agha, and T. A. Searles, Electromagnetically induced transparency control in terahertz metasurfaces based on bright-bright mode coupling, *Phys. Rev. B* **97**, 155403 (2018).
- [53] L. J. Sherry, S.-H. Chang, G. C. Schatz, R. P. Van Duyne, B. J. Wiley, and Y. Xia, Localized surface plasmon resonance spectroscopy of single silver nanocubes, *Nano Lett.* **5**, 2034 (2005).
- [54] S. Zhan, H. Li, Z. He, B. Li, Z. Chen, and H. Xu, Sensing analysis based on plasmon induced transparency in nanocavity-coupled waveguide, *Opt. Express* **23**, 20313 (2015).
- [55] T. Ma, Q. Huang, H. He, Y. Zhao, Xi Lin, and Y. Lu, All-dielectric metamaterial analogue of electromagnetically induced transparency and its sensing application in terahertz range, *Opt. Express* **27**, 16624 (2019).